IEEE Access
Multidisciplinary ⋮ Rapid Review ⋮ Open Access Journal

Received 20 June 2023, accepted 15 July 2023, date of publication 25 July 2023, date of current version 2 August 2023.

Digital Object Identifier 10.1109/ACCESS.2023.3298839

RESEARCH ARTICLE

A Novel Method for Detecting the Onset and Location of Mechanical Failure by Correlating Engineering Stress With Changes in Magnetic Properties of UNS S32205 Duplex Stainless Steel Using Quantum Well Hall Effect Sensors

FIREW ABERA BIRUU[1], PIERFRANCO RECCAGNI[2], DIRK ENGELBERG[2], AND MOHAMED MISSOUS[3], (Senior Member, IEEE)

[1]Ethronics, Institute of Robotics and Autonomous Systems (IRAS), Adama, Ethiopia
[2]Department of Materials, Metallurgy and Corrosion, School of Natural Sciences, The University of Manchester, M13 9PL Manchester, U.K.
[3]Department of Electrical and Electronic Engineering, School of Engineering, The University of Manchester, M13 9PL Manchester, U.K.

Corresponding author: Firew Abera Biruu (firew.abera@ethronics.org)

This work was supported in part the U.K.'s Engineering and Physical Sciences Research Council under Grant EPSRC-EP/LO22125/1, in part by the "UK Research Centre in Non-Destructive Evaluation (RCNDE3)", and in part by EP/P006973/1 "Future compound semiconductor manufacturing HUB."

ABSTRACT A new method for determining the onset and location of mechanical failure and the associated engineering stress via scanning the magnetic field distribution using a quantum-well Hall effect sensor is presented. From the Villari effect, it should be noted that changes in the magnetic properties of a ferromagnetic material should reflect some characteristics of the mechanical load and engineering stress that the material sustains. In this study, a direct relationship between the measured magnetic field, engineering proof stress (Rp0.2), and plastic deformation is revealed. The experiment was performed on a Grade 2205 duplex stainless steel under tensile loading. Magnetic field studies closely predicted the proof stress of the sample material. Consequently, the DC magnetic field response predicted the location of the plastic failure as early as 2% of the total strain. This new method has significant potential in systems that require condition monitoring and in-situ non-destructive testing to track the onset of plastic deformation in machine components.

INDEX TERMS Deformation, engineering stress, hall effect, magnetic field, magnetostriction, quantum well, Villari effect.

I. INTRODUCTION

Non-destructive Testing (NDT) involves various methods for detecting and evaluating defects in materials. NDT methods mainly concentrate on identifying flaws in structures and samples; however, these tests and investigations are mainly performed to identify failures that have already occurred. While NDT is mainly performed post defect, periodic check-ups during the lifespan of a component or a machine with associated diagnostics and prognostics are also done in related testing and evaluating scheme called Condition Monitoring (CM). Future NDT technologies should be integrated with tracking the onset of flaws, or better yet, should indicate changes in the properties of the material due to failure, to prevent catastrophic failure of the entire structure or system to which the part belongs. Therefore, it is important to create more opportunities to investigate the onset of failure of mechanical parts and members by studying their properties before irreversible damage occurs. One such quantity that is related to the material properties and can be held directly responsible for the failure of physical parts is the mechanical stress. The relationship between mechanical stress and magnetic behavior of engineering materials has long been established. The change in magnetic susceptibility

The associate editor coordinating the review of this manuscript and approving it for publication was Zhong Wu.

in different ferromagnetic materials owing to mechanical stress, known as the Villari Effect, has been studied by various researchers [1], [2], [3], [4].

The most common way to study mechanical stresses in electromagnetic NDT systems is by using inductance measurements, which are usually conducted by winding a coil around a magnetostrictive material and the target structure [5], [6]. In a different approach, Al-Hajjeh et al. [4] used the Villari effect phenomenon to demonstrate mechanical stress sensing by measuring the inductance change in Magnetostrictive Composite Material (MCM) sensors attached to the main target sample. A prototype magnetometer based on the Villari Effect was experimentally demonstrated by Wang and Feng [3], sensitivity of $18.8\text{pT}_{\text{rms}}/\sqrt{\text{Hz}}$, and a total noise of $40.3\text{pT}_{\text{rms}}$ from 0.1 to 10 Hz. Although the type of magnetovision system used has not been documented, Baudouin et al. [7] reported the results of investigations of changes in magnetic field properties after tensile deformation of silicon steel samples. While the report concluded that the magnetic field strength had significantly increased and magnetic properties were changed after stress was applied, further studies are required to connect changes in magnetic properties to its failure profile and to help determine parameters to pinpoint the onset of material failure.

The research reported in this paper uses a magnetic field-scanning technique called Magnetic Flux Leakage (MFL). As opposed to MFL applied to pure non-destructive testing systems, the flux leakage here is mainly exploited to study the change in magnetic field distribution on the surface of the sample as a result of continuous mechanical deformation.

Although a few sensors can be used to scan changes in magnetic field leakage, in this study, a Quantum Well Hall Effect (QWHE) sensor [8], [9] was used to directly measure the changes in the magnetic field at the surface of a sample during tensile loading. The results of using QWHE sensors for NDT applications were reported by Biruu et al. [10], [11]. Findings on magnetic field sensing around defects were also reported in [12], and the full research outcome of magnetic field scanning using QWHE sensors was reported in a PhD thesis [13]. Combining these findings, this paper here introduces a new technique in light of NDT and CM, based on established methods such as MFL and Villari Effect, by which it is possible to find a correlation between the applied tensile stress, magnetic properties, and the final location of the mechanical failure of the sample.

II. THEORETICAL BACKGROUND

A. THE VILLARI EFFECT

The Villari effect, also known as inverse magnetostriction, occurs when ferromagnetic materials are subjected to a mechanical loading. Based on the magnetic properties of the material and the loading type, as discussed in [14], the magnetization increases or decreases, and the origin of the magnetic properties of materials can be explained as the result of the magnetic moments of atoms, in which the two main contributors to the magnetic properties of a material are thought to be the electron spin and orbital motion of electrons. An electric current is the motion of an electron, and, as such, the circular path of the electron around the orbit is synonymous with a current loop. This current loop acts as an elementary magnet with a magnetic moment, and the total magnetic moment of an atom originates from the contribution of the magnetic moment of each electron. The dipole moments of the accumulation of uncompensated electron spins contribute to the magnetic moment in an atom, but these often cancel each other, resulting in the loss of the permanent magnetic moment. These atoms undergo changes in their orbital motion to acquire induced magnetic moments when placed in a magnetic field. This is referred to as the magnetic susceptibility. The dimensionless magnetic susceptibility, X_ν relates the magnetization B to the magnetic field strength H as follows:

$$\text{B} = \mu_{\text{o}} H\,(1 + \text{X}_\nu) \tag{1}$$

where μ_{o} is the permeability of free space

Equation (1) indicates that the magnetic susceptibility is directly related to the magnetization field. Changes in susceptibility would directly affect the magnetization limit of a material. This effect has also been observed by Salach et al. [14] studied the tensile and compressive stress dependence of a $\text{Fe}_{25}\text{Ni}_{55}\text{Si}_{10}\text{B}_{10}$ magnetic core. Their study found that, for compressive stress, the magnetization of the core increased, whereas it decreased for tensile stress.

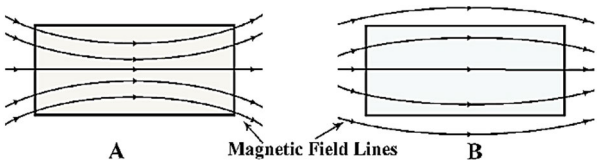

FIGURE 1. Magnetic flux around (A) Ferromagnetic material and (B) diamagnetic material.

Theoretically, for a constant source of magnetizing field, it is expected that the change in the susceptibility of the specimen changes the intensity of the magnetic field near the specimen boundaries. This is because, when the specimen is more susceptible, it exhibits increased paramagnetic properties, and when it is less susceptible, it mimics diamagnetic properties, as shown in Figure 1.

B. THE HALL VOLTAGE

When a current-carrying conductor, or conveniently a two-dimensional object such as a sheet of metal depicted in Figure 2, is placed under a uniform magnetic field normal to the electric field, the Lorentz Force creates a potential difference perpendicular to both the electric and magnetic fields. This potential is the Hall Voltage V_H, and the Hall Effect is named after American Physicist Edwin H Hall.

The Hall voltage is given by:

$$V_H = kAI \tag{2}$$

where k is the sensitivity of the QWHE sensor, A the total circuit gain, and I the sensor bias current.

As can be seen from equation (2), the Hall voltage strength is directly proportional to the bias current, which varies with the strength of the normal B-field. The stronger the B-field owing to the MFL resulting from deformation, the stronger the corresponding V_H.

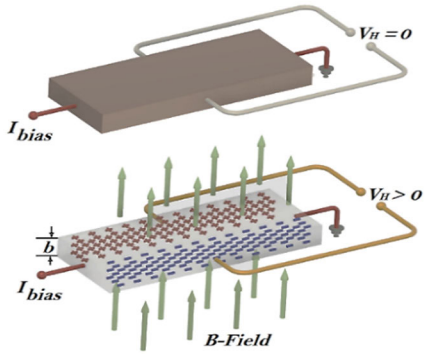

FIGURE 2. A conductive media like a sheet of metal (or a 2-dimensional Electron gas in a QWHE sensor) experiences the Hall Effect (with a Hall Voltage, VH), when placed in a uniformly distributed orthogonal magnetic field.

C. THE QUANTUM WELL HALL EFFECT SENSOR

There are various ways to sense MFL signals. The most common sensors can be summarized as AMR/GMR, superconducting quantum interference devices (SQUID), Coils and Hall effect sensors. The sensor used to develop the magnetometer in this experiment was a special type of Hall Effect sensor called the P2A quantum well Hall effect (QWHE) sensor, whose properties have been reported in detail in [8] and [9].

QWHE sensors are based on III-V semiconductor materials. When two semiconductors with varying energy bandgaps are brought into the heterojunction, there exists a quantum well in which charge carriers are trapped and have quantized energy levels. This restricts the flow of charge carriers in only two dimensions, also called a 2-Dimensional Electron Gas (2DEG), which increases the mobility of electrons and, consequently, the sensitivity of the sensor.

The choice of the AHS P2A QWHE sensor was based on a comparison of the three most sensitive silicon-based commercial Hall Effect sensors made by Allegro (A1324), Melexis (MLX90242), and Honeywell (SS39ET). These linear sensors had sensitivities of 50, 39, and 14 mV/mT, respectively, with a cutoff frequency of 10 kHz. The minimum detectable magnetic fields by these sensors in a 10 Hz bandwidth are 864, 6500, and 652 nT, respectively [15], [16], [17], Sadeghi et al. [9] demonstrated that QWHE sensors had an overall circuit sensitivity of 533 mV/mT biased at 1 mA. This is a factor of 10, 13, and 37 higher than those of the Allegro (A1324), Melexis (MLX90242), and Honeywell (SS39ET) devices, respectively. Additionally, QWHE sensors were found to have low power consumption of only 10.4 mW, as opposed to the power consumption of the Honeywell SS39ET, Allegro A1324 and Melexis MLX90242 ICs, which are 30 mW, 34.5 mW and 12.5 mW at 5 V supply, respectively. Other advantages of the P2A QWHE sensors used in this work include low bias current requirement, highly reduced circuitry, extended operating temperature range from −100°C to 200°C and small linearity error of the Hall voltage [18].

III. METHODOLOGY AND EXPERIMENTAL SETUP

A. METHODOLOGY

The sample chosen for both the DC and AC B-field experiments was duplex stainless steel of grade 2205. Duplex stainless steels are characterized by a ferritic-austenitic microstructure with approximately equal proportions of the two phases. It has good mechanical and corrosion characteristics [19]; therefore, it is used in marine, nuclear, and chemical industries. The selection of this material was a paramount feature of this study. As shown in Figure 3, it contains both ferromagnetic properties from the ferritic phase and nonferromagnetic properties from austenitic phases, which makes changes in the susceptibility property of the material depicted in Figure 1 more contrasted and 'visible' to the QWHE sensors.

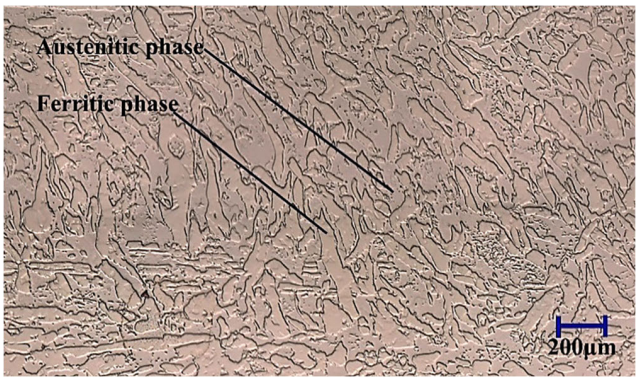

FIGURE 3. Micrograph of the duplex stainless steel at X200 magnification showing austenitic and ferritic phases.

The following methodology was followed to carry out the experiment. The duplex stainless steel was machined to a thickness of 1 mm, and to general dimensions and shapes as shown in Figure 5. The 30 mm gauge on the sample was divided into 15 equal divisions every 2 mm. Each sample was held in a Deben 5kN miniature tensile tester. Both ends of the sample were illuminated with a 320mT magnetic field using button magnets. The magnets were reversed for field lines continuity. The secured sample was then stretched with intermittent tensile loading. The miniature tester was stopped to measure the magnetic field at the 15 segments and elongations of 0%, 0.2%, 0.5%, 1.6%, 2%, 2.4%, 10%, 22%, 24% and 24.5%.

The magnetic field measurement at each elongation and the tensile stress values were recorded, analyzed and plotted. Comparison between magnetic fields before and after the material's theoretical proof stress were then made as detailed in section IV below. Other important results were explained and the relationship between proof stress, the material failure and related magnetic field measurements were also explained in comparison to existing magnetic field property around a defect.

B. EXPERIMENTAL SETUP

The experimental setup, where the duplex specimen was held between the jaws of the tensile stress testing device, is shown in Figure 6, with the simplified magnetic circuit shown in Figure 10. After applying the tensile load up to a predetermined elongation, the load was temporarily suspended, as shown by the shallow drop in the load curve in Figure 8.

FIGURE 4. QWHE sensor based magnetometer, designed and developed at the university of manchester, used in the research.

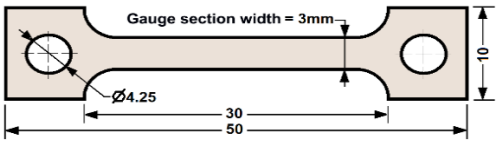

FIGURE 5. Duplex stainless-steel grade 2205 sample shape and dimensions. All dimensions in mm. Note: Drawing not to scale.

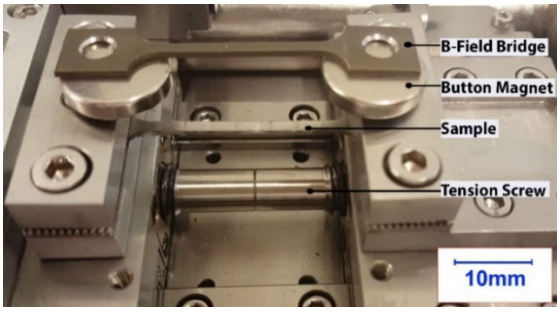

FIGURE 6. Sample and B-Field bridge orientation within the deben 5kN material miniature tensile tester.

After applying the tensile load up to a predetermined elongation, the load was suspended, as shown by the shallow drop in the load curve in Figure 8. Using the QWHE sensor-based magnetometer shown in Figure 4, the DC magnetic field was measured 1 mm above the surface of the sample before the tensile force was applied again to increase the strain to the next measurement point. The 1 mm stand-off is the physical constraint of the sensor package, as shown in Figure 7. The experiments were conducted using three

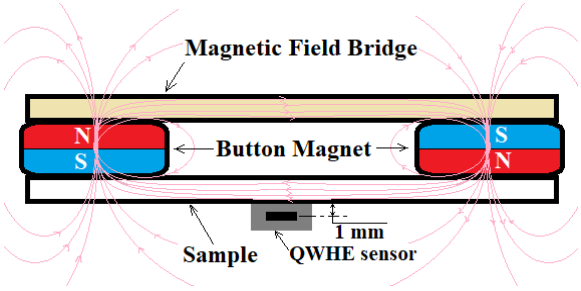

FIGURE 7. Simplified magnetic circuit.

identical samples. In sample 1, up to 25 predetermined elongation points were considered, distributed over the elastic, elastic-to-plastic transformation, and plastic regions. After analyzing the results of Sample 1, further confirmatory measures were made on the selected elongation points on Samples 2 and 3.

Ultimate tensile stresses of up to 574, 641, and 608 MPa were induced in samples 1, 2, and 3, respectively, by taking the samples to a maximum elongation of up to 24.5% for sample 1 and 22% for samples 2 and 3, respectively, using an extension rate of 0.3 mm/min. The test was stopped at this elongation, as further extension would take the specimen close to failure, which would take the research out of its scope. As the magnetic flux requires a closed loop to force it to loop back into the specimen, a similar Duplex B-Field bridge was used between the button magnets, which biased the sample with a constant B-Field of 320mT.

Figure 8 shows three sections of the deformation process. In the elastic region between 0% and 2% elongation on the strain axis, the deformation was almost linearly related to the stress in the specimen. The second and most relevant stage was the plastic region, which was between 2% and 22% elongation. The plastic region was the region where the specimen underwent permanent physical changes. The difference between the sustained stress and stress level after the load is removed for the B-field measurement is notable in the segmented parts below the nominal stress–strain curve. The third stage is the necking region, which shows 22% elongation on the strain axis. The tensile test was stopped at 24.5% elongation for sample 1 and at any point after 22% elongation for samples 2 and 3, after which total failure of the specimen would occur, which was not within the scope of this research.

IV. RESULTS AND DISCUSSION

The measured magnetic field across the duplex specimen for elongation within the elastic region of Sample 1 is shown in Figure 9. The black curve at 0% shows the magnetic field when the specimen was held in place in the tensile stress machine without applying any force. This curve was used as a reference. The red and dark blue solid lines represent the results at 0.2% and 0.5% elongations on the strain axis, respectively. Similar measurements were performed for

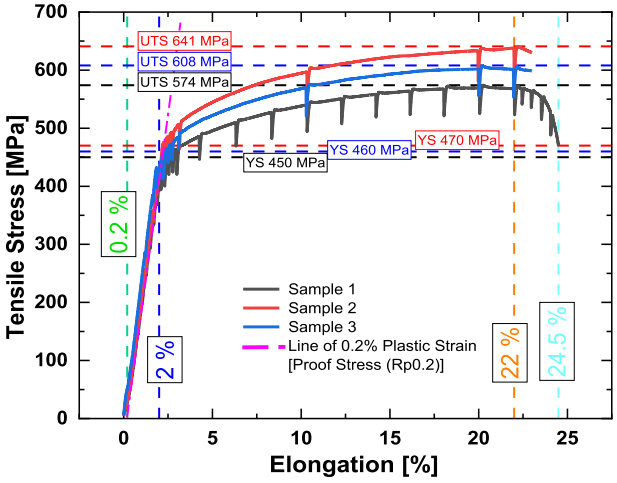

FIGURE 8. The stress-strain curve showing important sections of the deformation parts for duplex stainless steel grade 2205. The load drops show the points where the extension was stopped for analysis.

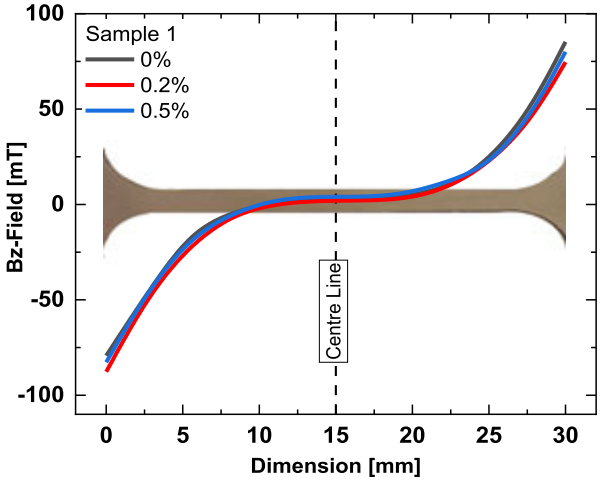

FIGURE 9. DC magnetic field measured across the specimen length at 0%, 0.2% and 0.5% elongation.

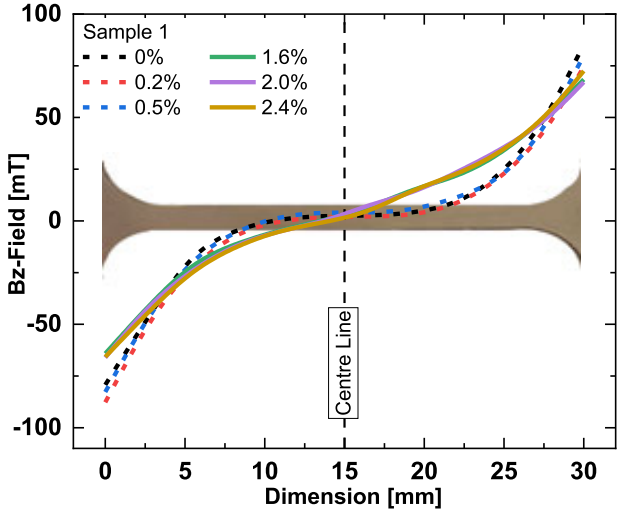

FIGURE 10. Measured B-Field before Proof Stress at 0%, 0.2% and 0.5% and thereafter at 1.6%, 2% and 2.4% leading from elastic to plastic state transformation in sample 1.

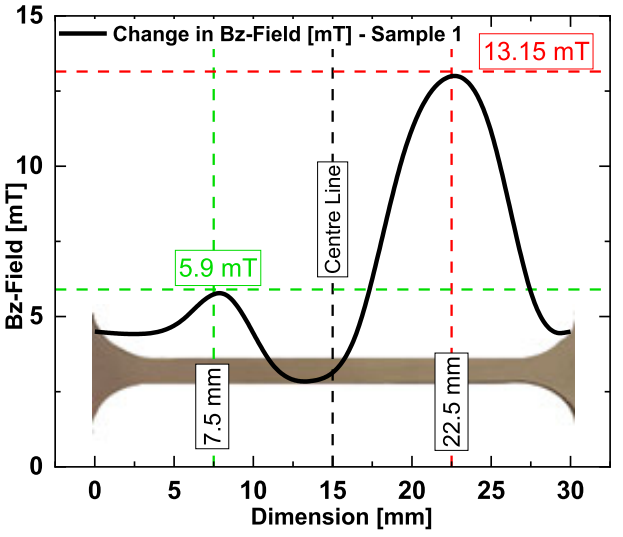

FIGURE 11. Absolute change in B-Field immediately before and after Proof Stress in sample 1.

samples 2 and 3, as shown in Figure 12 and Figure 14, respectively. The solid curves in these figures show the magnetic field distribution before the onset of a unique stress level, which was designated as the proof stress. Proof stress is a term used to describe the stress that causes permanent extension of the sample, transforming the deformation from an elastic to a plastic state. This is usually taken from an offset of approximately 0.2% of the linear curve into plastic strain. This corresponds to 2% of the strain curve in Figure 8, and the values were approximately 450MPa, 470MPa and 460MPa for samples 1, 2, and 3, respectively. Below the proof stress, for 0.2% and 0.5% elongation, we observed a negligible variation in the magnetic field from the 0% elongation B-field curve.

Two groups of curves are compared in Figure 10, Figure 12 and Figure 14. The dotted curves show the magnetic field distribution before the proof stress, and the solid group of curves shows the magnetic field distribution immediately after the proof stress is passed, which is close to the elastic-plastic boundary. For all three samples, a stark difference can be observed between the dotted group of curves measured before the transition at 0%, 0.2%, and 0.5% and that of the solid group of curves measured after the transition at 1.6%, 2.0%, and 2.4% elongations, with a higher magnetic field measured in the latter group of curves after the transition.

The fact that a higher magnetic field is registered at the elastic-plastic transition can be interpreted as a general increase in the magnetic field intensity at the surface of the sample. As the stress increased inside the sample, the positive magnetostriction decreased the saturation field of the specimen. Part of the sample effected by the tensile force

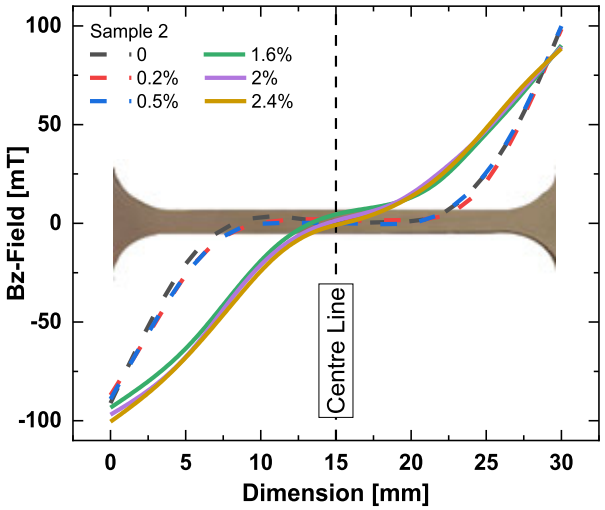

FIGURE 12. Measured B-Field before Proof Stress at 0%, 0.2% and 0.5% and thereafter at 1.6%, 2% and 2.4% leading from elastic to plastic state transformation in sample 2.

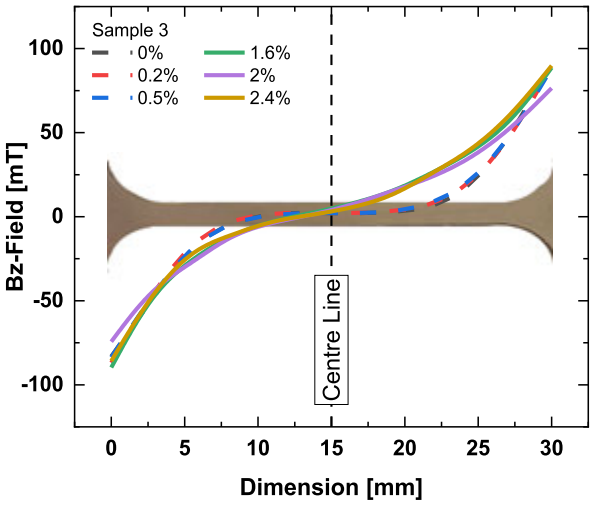

FIGURE 14. Measured B-Field before Proof Stress at 0%, 0.2% and 0.5% and thereafter at 1.6%, 2% and 2.4% leading from elastic to plastic state transformation in sample 3.

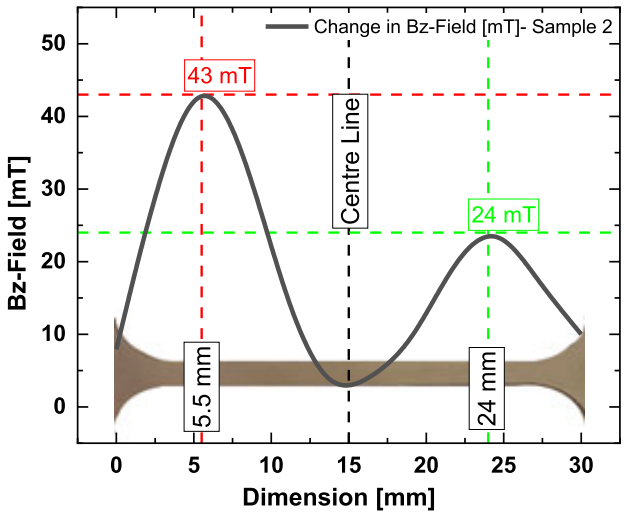

FIGURE 13. Absolute change in B-Field immediately before and after Proof Stress in sample 2.

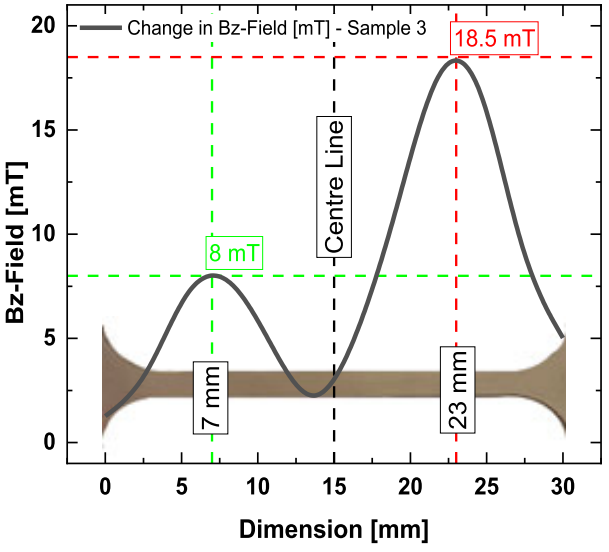

FIGURE 15. Absolute change in B-Field immediately before and after Proof Stress in sample 3.

as a result goes 'locally' diamagnetic and this increases the detectable B-field at the outer surface of the specimen as the reduced saturation forces out the magnetic flux. This behavior is mainly significant within the gauge section of the sample, as it is the main area of failure. The changes in the B-field results between the two groups of values shown in Figure 10, Figure 12 and Figure 14, that is, the changes in the B-field before and after the proof stress, are shown in Figure 11, Figure 13 and Figure 15. This was calculated by taking the difference between the average values before the proof stress at 0%, 0.2%, and 0.5%, and thereafter at 1.6%, 2%, and 2.4%.

For Sample 1, Figure 11 shows at the right of the Centre reference line around 22.5 mm on the horizontal line, the maximum change in B-Field registered is 13.15mT, and at the left of Centre Line, the absolute maximum change at around 7.5 mm in the sample's gauge section is 5.9mT. A significant contrast is observed between the left and right side of the Centre Line, with the right side – the side that would fail, registering more than twice change in B-Field than the left. In both Samples 2 and 3, the absolute change between the measurements just before the poof stress and that after the proof stress correctly showed the direction of the failure. In Sample 2, Figure 13, maximum Bz-field of 43 mT at 5.5 mm at the left of the Centre-Line as opposed to 24 mT at 22.5 mm, and in Sample 3, Figure 15, a maximum Bz-field of 18.5 mT at 23 mm at right of the Center-line as opposed to 8 mT at 7 mm.

Generally, the increase in the measured B-field continued with an increase in strain. This is shown in Figure 16,

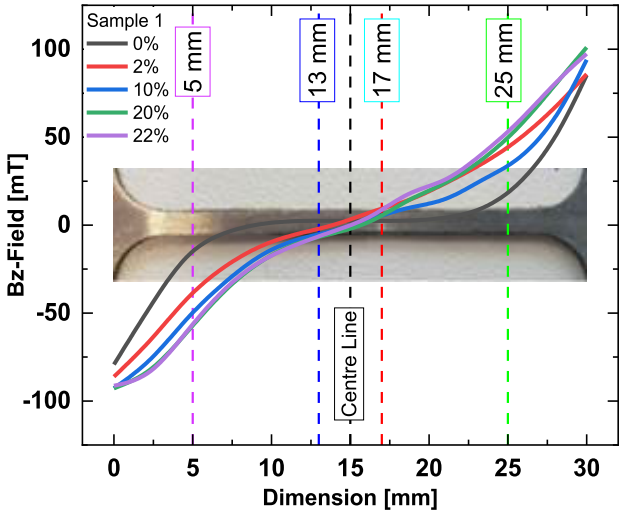

FIGURE 16. Increase in B-Field with increase in strain. Measured B-Field at 0%, 2%, 10%, 20% and 22% elongation for sample 1.

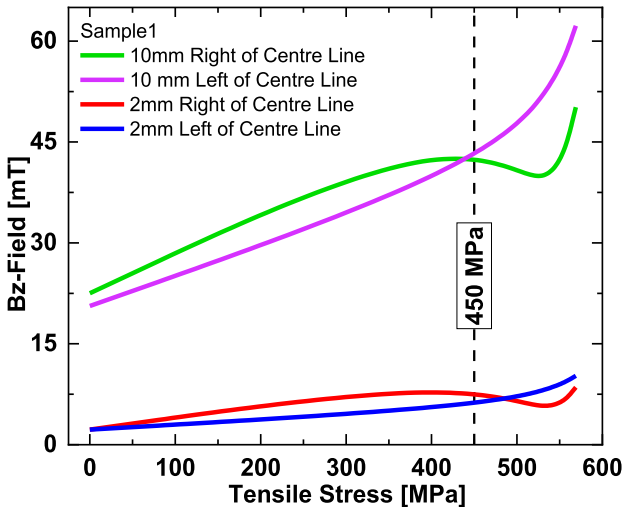

FIGURE 17. Measured B-field against tensile stress, at 2mm and 10mm on opposite side of the centre line for sample 1. Note: The relative positions of the selected points are shown in Figure 16.

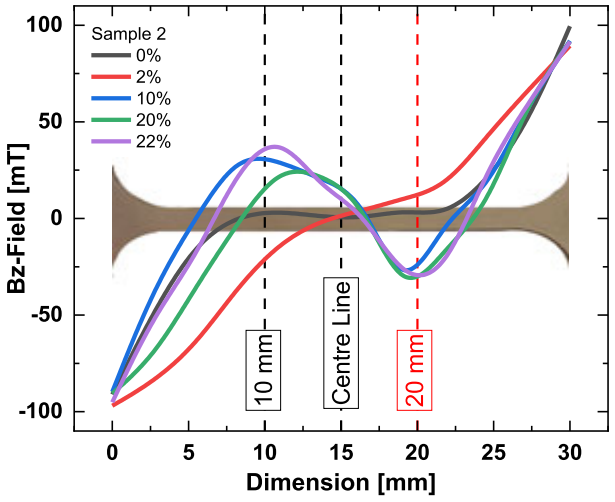

FIGURE 18. Increase in B-Field with increase in strain. Measured B-Field at 0%, 2%, 10%, 20% and 22% elongation for sample 2.

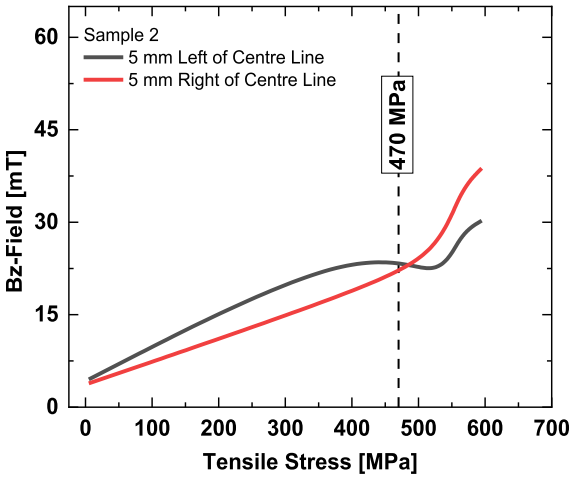

FIGURE 19. Measured B-field against tensile stress, 5mm on opposite side of the centre line for sample 2. Note: The relative positions of the selected points are shown in Figure 18.

Figure 18 and Figure 20 for additional curves within the plastic deformation region at elongations of 10%, 20%, and 22% for samples 1, 2, and 3, respectively. Additional information observed in these regions is that, unlike the elastic to plastic transformation measurements, these curves are no longer smooth and predictable, and the nonlinearity of the magnetic field sensor near the button magnets is observed at each end of the curves.

These irregularities observed at the failure side of the centerline signify that the necking span of the specimen could have started at the failure sides identified in Figure 11, Figure 13 and Figure 15. The relationship between the stress that causes these failures and the measured Bz-field was studied by taking two pairs of comparison points in sample 1 and a further pair of points in samples 2 and 3.

In sample 1, the first pair of points are each 10 mm away from the centerline; one at the 5 mm position on the dimension axis, shown as a purple line at the left and the other at 25 mm in green at the right of the centerline. The second pair of points was 2 mm from the centerline. The points are at 13 and 17 mm on the dimension axis shown by the blue and red lines, respectively. Figure 17 depicts the comparison of the Bz-field measured at these corresponding points as, that is, 5, 13, 17, and 25 mm, as the tensile loading gradually increases.

Two important observations can be made from Figure 17. The first is the increase in B-Field on the side of the failure, that is, 2 mm and 10 mm to the right of the center line, both above their counterparts from the left.

The second is the gradual decrease in the measured Bz-field around the proof stress value; for sample 1, this

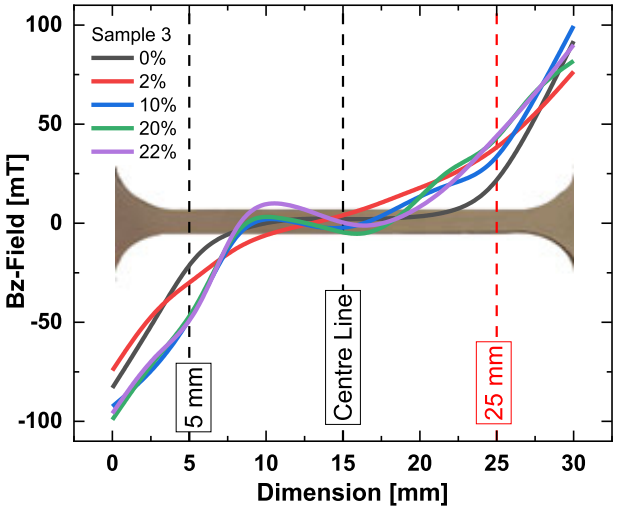

FIGURE 20. Increase in B-Field with increase in strain. Measured B-Field at 0%, 2%, 10%, 20% and 22% elongation for sample 3.

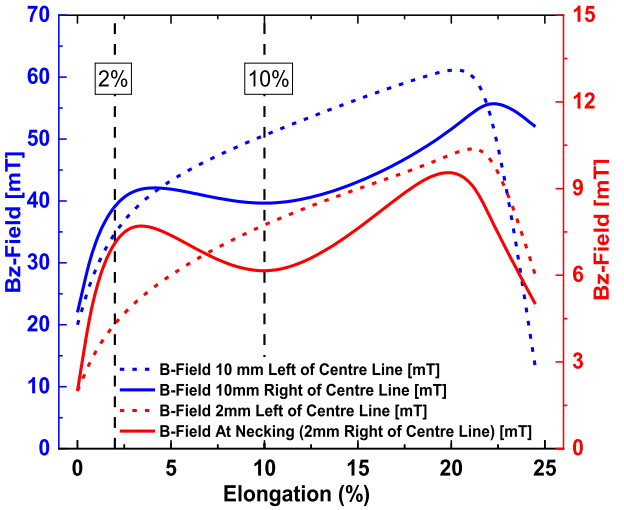

FIGURE 22. Measured B-field against elongation for data points shown in Figure 16.

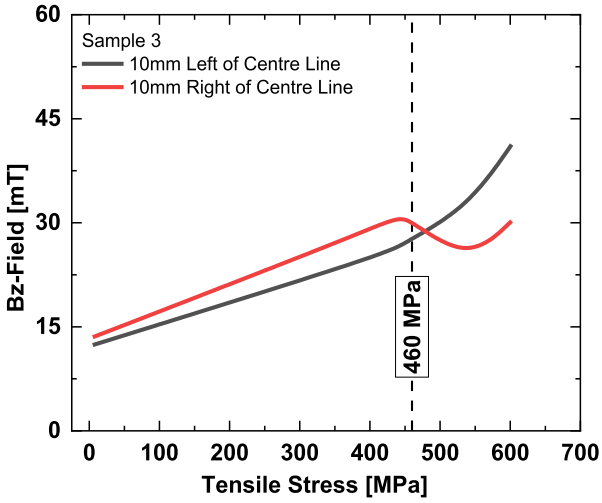

FIGURE 21. Measured B-field against tensile stress, at 10mm on opposite side of the centre line for sample 3. Note: The relative positions of the selected points are shown in Figure 20.

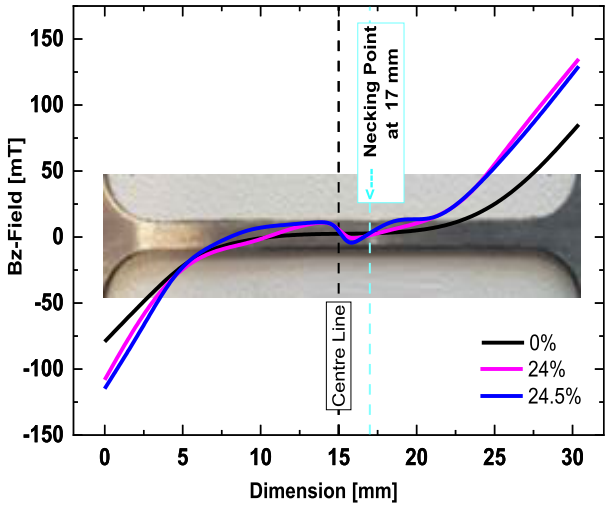

FIGURE 23. DC magnetic field measured in the necking region across the specimen length at 24% and 24.5% elongation compared with results at 0%.

was 450 MPa. Two more pairs of points, 5 mm left and right of the centerline in sample 2, Figure 18, and 10 mm left and right of the centerline in sample 3, Figure 21, were also considered. In both cases, the Bz-field against the increasing tensile stress is shown. In all three cases, having superimposed the proof stress values we have from Figure 8 to the result curves in Figure 17, Figure 19 and Figure 21, it can be seen that the proof stress values are very close to the intersection of the curves in each graph. The proof stresses, i.e., the materials' Yield Strengths of 450, 470, and 460 MPa, could be determined from these curves for Samples 1, 2, and 3, respectively.

There are several points of interest for future research. For instance, two pairs of curves show the comparison in measured B-Field between the failure side - Right Side, and the 'normal' side – Left Side of the Center Line, in Figure 22. As elongation progressed, the Bz-Field at each of these locations was tracked and compared with their counterparts in the opposite direction. The blue set of curves compares the B-field at 10 mm from the opposite sides of the centerline, whereas the red curves show those at 2 mm.

In Figure 22, the measured B-Field from the failure side remain higher than those points from the 'normal' side, before proof stress. However, once the Yield Stress was passed, the B-field began to weaken until the 10% elongation point was reached. As shown in Figure 17, Figure 19and Figure 21, the B-field lines bend down to pass through an irreversible point of the deformation – the Yield Stress. Similarly, the B-Field lines here are also indicative of another significant phenomenon – an irreversible life span of the sample that will lead to necking and failure.

The necking points are shown in Figure 23. Theoretically, a local magnetic pole inversion of the Bz field is expected around defects [20]. As the necking point developed into a significant defect in the cross-sectional area of the gauge

section of the specimen, this property was observed in the Bz-field curve. The local magnetic field polarity inversion that occurred at 24% elongation and more significantly at 24.5% was captured by the QWHE sensor. This inversion is centered exactly at the core of the necking at the 17 mm mark on the horizontal axis.

V. CONCLUSION

A novel method for scanning and predicting the mechanical stress levels that lead to failure was presented. This Method uses small, compact, portable, low-power-dissipation quantum-well Hall effect sensors to directly measure the normal component of the magnetic field changes owing to the Villari effect of a sample that undergoes deformation under engineering stress.

The experimental results demonstrated a relationship between the measured magnetic field, proof stress, stress at which the specimen begins deformation, and the elastic and plastic deformation zones. Although it was clear experimentally that the magnetic field measured immediately after the proof stress was significantly higher, it was also possible to magnetically predict when the proof stress occurred. By comparing the opposite sides of the center of the sample, it was observed that the failure side experienced more than twice ($>100\%$) the increase in the magnetic field than the 'normal' side. Furthermore, it was possible to detect a point at approximately 10% elongation, as shown in Figure 22, in the plastic region where the magnetic field reached a local low point before it reversed. Although local magnetic field inversion is known to indicate discontinuity or flaws, we suspect that it is also an indication of permanent deformation prior to failure. This phenomenon will be a part of future research.

The most important outcomes are the ability to track failure-causing stresses and predict areas where possible failure can occur around the elastic-to-plastic transition point. As a result, by studying the relationship between the tensile stress and the measured B-field at the failure site, it is also possible to determine when a given sample has approached or just passed its yield strength.

This novel method could play a significant role in systems that require condition monitoring and in-situ nondestructive testing. Accurately predicting where a material is likely to fail at only 2% of its total elongation can prevent catastrophic failure of machine components. This method can also be applied to map 2D to 3D arrays when coupled with highly sensitive sensors such as the QWHE sensors used in this experiment.

REFERENCES

[1] C. Appino, F. Fiorillo, and A. Maraner, "Initial susceptibility vs. applied stress in amorphous alloys with positive and negative magnetostriction," *IEEE Trans. Magn.*, vol. 29, no. 6, pp. 3469–3471, Nov. 1993.

[2] M. J. Dapino, R. C. Smith, and A. B. Flatau, "Structural magnetic strain model for magnetostrictive transducers," *IEEE Trans. Magn.*, vol. 36, no. 3, pp. 545–556, May 2000.

[3] H. B. Wang and Z. H. Feng, "A highly sensitive magnetometer based on the Villari effect," *IEEE Trans. Magn.*, vol. 49, no. 4, pp. 1327–1333, Apr. 2013.

[4] A. Al-Hajjeh, E. Lynch, C. T. Law, and R. El-Hajjar, "Characteristics of a magnetostrictive composite stress sensor," *IEEE Magn. Lett.*, vol. 7, pp. 1–4, 2016.

[5] J. Olivera, M. Gonzalez, J. V. Fuente, R. Varga, A. Zhukov, and J. J. Anaya, "An embedded stress sensor for concrete SHM based on amorphous ferromagnetic microwires," *Sensors*, vol. 14, no. 11, pp. 19963–19978, Oct. 2014.

[6] M. Wun-Fogle, H. T. Savage, and A. E. Clark, "Sensitive, wide frequency range magnetostrictive strain gage," *Sens. Actuators*, vol. 12, no. 4, pp. 323–331, Nov./Dec. 1987.

[7] P. Baudouin, Y. Houbaert, and S. Tumanski, "Magnetic local investigations of non-oriented electrical steels after tensile deformation," *J. Magn. Magn. Mater.*, vols. 254–255, pp. 32–35, Jan. 2003.

[8] N. Haned, "Nano-tesla magnetic field magnetometry using an InGaAs–AlGaAs–GaAs 2DEG Hall sensor," *Sens. Actuators A, Phys.*, vol. 102, no. 3, pp. 216–222, Jan. 2003.

[9] M. Sadeghi, J. Sexton, C.-W. Liang, and M. Missous, "Highly sensitive nanotesla quantum-well Hall-effect integrated circuit using GaAs–InGaAs–AlGaAs 2DEG," *IEEE Sensors J.*, vol. 15, no. 3, pp. 1817–1824, Mar. 2015.

[10] F. A. Biruu, J. Sexton, C. W. Liang, and M. Missous, "An automated two-dimensional magnetic field scanner based on quantum well hall effect sensor for non-destructive testing," presented at the 57th Annu. Brit. Conf., Brit. Inst. for Non-Destructive Test., Northampton, U.K., Sep. 10, 2018.

[11] J. M. Watson, C. W. Liang, J. Sexton, F. A. Biruu, and M. Missous, "Surface-breaking flaw detection in mild steel welds using quantum well hall effect sensor devices," presented at the 45th Annu. Rev. Prog. Quant. Nondestruct. Eval., QNDE, May 8, 2019.

[12] F. A. Biruu, E. Balaban, E. Ahmad, C. W. Liang, and M. Missous, "2D magnetic field sensing around defects in ferromagnetic and non-ferromagnetic materials using 2DEG Quantum Well Hall Effect sensor arrays," in *Proc. 56th Annu. Conf. Brit. Inst. Non-Destructive Test. (NDT)*, 2017, pp. 496–509.

[13] F. A. Biruu, "High sensitivity two-dimensional electron gas (2DEG) Quantum Well Hall Effect sensors for novel pre-failure engineering stress analysis and non-destructive testing systems," Dept. Elect. Electron. Eng., School Eng., Univ. Manchester, Manchester, U.K., Tech. Rep. uk-ac-man-scw:324437, 2020.

[14] J. Salach, R. Szewczyk, A. Bieńkowski, and P. Frydrych, "Methodology of testing the magnetoelastic characteristic of ring-shaped cores under uniform compressive and tensile stresses," *J. Electr. Eng.*, vol. 61, no. 7s, pp. 93–95, 2010.

[15] *A1324, A1325 and A1326 Low Noise Linear Hall Effect Sensor ICs with Allegro Output*, Allergo, Poland, U.K., Sep. 2013.

[16] *MLX90242 Linear Hall Effect Sensor*, Melexis, Bevaix, Switzerland, Feb. 2012.

[17] *SS39ET/SS49E/SS59ET Linear Hall-Effect Sensor ICs*, Honeywell, Morrisontown, NJ, USA, Mar. 2013.

[18] *Highly Sensitive Hall Effect Sensor P2A Rated at 160 V/AT*, AHS Advanced Hall Sensors Ltd, Stretford, England, 2015.

[19] C. Örnek and D. L. Engelberg, "Correlative EBSD and SKPFM characterisation of microstructure development to assist determination of corrosion propensity in grade 2205 duplex stainless steel," *J. Mater. Sci.*, vol. 51, no. 4, pp. 1931–1948, Feb. 2016.

[20] V. Suresh and A. Abudhahir, "An analytical model for prediction of magnetic flux leakage from surface defects in ferromagnetic tubes," *Meas. Sci. Rev.*, vol. 16, no. 1, pp. 8–13, Feb. 2016.

FIREW ABERA BIRUU received the M.Eng. degree (Hons.) in mechatronic engineering and the Ph.D. degree in electrical and electronic engineering from The University of Manchester, Manchester, U.K., where he worked on advanced nanotesla III–V 2DEG quantum well Hall Effect sensors and novel applications. He is currently the Founder and the CEO of Ethronics, Institute of Robotics and Autonomous Systems (IRAS), Adama, Ethiopia, a robotics and autonomous systems institute. His research interests include pre-failure mechanical stress scanning and analysis, the design of Hall Effect linear array magnetometer and multidimensional robotic magnetic field scanning, analog and digital circuits, and applications of robotic and autonomous systems.

PIERFRANCO RECCAGNI received the Ph.D. degree. He is currently a Research Engineer in corrosion protection and metallurgy. He is an experienced Laboratory-Based Researcher both in industry and in academia with an extensive knowledge of materials microstructure/properties characterization (with a particular interest in high-resolution techniques, such as SEM and AFM). His background is in materials and corrosion science for oil and gas and automotive industries, with a particular interest in materials processing and environment-assisted degradation mechanisms.

DIRK ENGELBERG received the Dipl.-Ing. (FH) degree in surface engineering and materials science from Aalen University, Germany, the M.Sc. degree in corrosion science and engineering from the UMIST, U.K., and the Ph.D. degree in metallurgy and materials science from The University of Manchester, U.K. He is currently a Professor of materials performance and corrosion with The University of Manchester. In the Department of Materials, he is a Fellowship Mentor, the Line Manager (Hard Materials), and the Metallurgy and Corrosion Theme Lead. He has broad expertise in steel metallurgy, microstructure and grain boundary engineering, corrosion/electrochemistry, and the application of in-situ/in-operando characterization techniques, including X-ray computed tomography and 2D/3D correlation methods, with a keen interest in the development and application of novel material characterization techniques and methods. He has over 15 years of experience in leading energy-related research projects, with a focus on developing robust and resilient approaches for the prediction, simulation, and mitigation of corrosion and environment-assisted cracking in radwaste storage/disposal facilities, petrochemical environments, and for hydrogen sustainability applications.

MOHAMED MISSOUS (Senior Member, IEEE) is currently a Professor of semiconductor materials and devices with the School of Electrical and Electronic Engineering, The University of Manchester. His research activities are centered on the growth of complex multilayer semiconductor films by the technique of molecular beam epitaxy (MBE). He has established a large MBE and the Compound Semiconductor Laboratory for materials growth, assessment equipment, compound semiconductor processing facility, and device testing. Over the years, he has concentrated with considerable success, on establishing practical approaches and techniques required to meet stringent doping and thickness control, to sub-monolayer accuracy, for a variety of advanced quantum devices, from room temperature operating mid-infrared quantum well infrared photodetectors, NanoTesla magnetic imaging using ultrasensitive 2DEG for nondestructive testing, and 77 GHz car radars to Terahertz materials for 1.55 μ imaging. He is also concentrating on the manufacturability of quantum devices including tunnel structures. His involvement in the above research topics has led to the publication of over 240 papers in the open, international literature. He is a fellow of the Royal Academy of Engineering, the Institute of Physics, and IET. He was a recipient of the 2015 Royal Society Brian Mercer Award for the manufacturability of tunnel devices together with Prof. M. Kelly. He is regularly invited to give talks at international venues on mm-wave and THz technologies.